# Optimized energy coupling at ultrafast laser-irradiated metal surfaces by tailoring intensity envelopes: Consequences for material removal from Al samples

J. P. Colombier,[1] P. Combis,[2] A. Rosenfeld,[3] I. V. Hertel,[3,*] E. Audouard,[1] and R. Stoian[1,†]
[1]*Laboratoire TSI (UMR 5516 CNRS), Université Jean Monnet, 42000 Saint Etienne, France*
[2]*CEA/DAM Ile de France, Dept. de Physique Théorique et Appliquée, 91680 Bruyères-le-Châtel, France*
[3]*Max-Born-Institut für Nichtlineare Optik und Kurzzeitspektroskopie, 12489 Berlin, Germany*
(Received 20 June 2006; revised manuscript received 20 September 2006; published 18 December 2006)

We present results describing the efficiency of energy coupling in laser-irradiated metallic surfaces by ultrashort laser pulses with different intensity envelopes. Subsequently, we discuss probable thermodynamic paths for material ejection under the laser action. Ion and neutral emission from the excited sample is used as a sensitive method to probe the efficiency of energy deposition in the material. With support from numerical simulations of the hydrodynamic advance of the excited matter, consequences of optimized energy coupling relevant for applications in material processing are revealed. Despite the reduced sensitivity to intensity-dependent effects for linear materials, the overall absorption efficiency can be elevated if the proper conditions of density and temperature are met for the expanding material layers. In this respect, short sub-ps single pulse irradiation is compared with picosecond sequences. We show that in particular irradiation regimes, characterized by fluences superior to the material removal threshold, laser energy delivery extending on several picoseconds leads to significant superheating of the superficial layers as compared to femtosecond irradiation and to a swift acceleration of the emitted particles. Subsequently, the lifetime of the post-irradiation liquid layer is diminished, which, in turn, translates into a reduction in droplet ejection. In contrast, short pulse irradiation at moderate fluences generates a higher quantity of removed material that is ejected in a dense mixture of gas and liquid-phase particulates.

DOI: 10.1103/PhysRevB.74.224106 PACS number(s): 61.80.−x, 79.20.Ds, 52.50.Jm, 64.70.Dv

## I. INTRODUCTION

Ultrafast laser technology becomes increasingly important in practical cross-sectorial applications such as in material processing. The degree of precision in laser-machined structures is a determinant for many end-user applications. Several reports have emphasized the "athermal" character of laser excitation in a regime where material removal occurs, and have underlined consequences for increasing precision in laser machining. Reports[1,2] based on *ex situ* examination of the irradiated region have highlighted the appearance of sharp, well-defined structures, subsequent to an ultrafast laser-induced quasi–solid-to-plasma transition. Clear advantages for femtosecond irradiation in micromachining and, potentially, in nanomachining were indicated and explained based on several facts, such as the strong energy localization, the absence of the recast layer, and the efficiency of material removal. The primary transformation phases just following laser excitation were observed by several experimental methods, including transient optical measurements[3] or interferometric techniques,[4] stressing the role of laser-induced shocking in triggering material transformations. Other works were concerned with the characteristic of the ablation products in the ultrafast irradiation regimes.[5] The plasma plume was analyzed spectrally[6] and kinetically,[7–9] and time-of-flight techniques[10–12] were employed to indicate a certain nonthermal character in the kinetic properties of the plume. Ultrashort pulse laser ablation in the sub-ps range was connected with a high efficiency of nanoparticulates production.[12–16] A summary of these results points to several characteristics of the ultrafast irradiation regime: fast charge particle distribution, clean emission spectra, or the appearance of nano-aggregates in the ablation products, either in "gas-phase" or collected on substrates in pulse laser deposition techniques. These later products are partly generated by liquid-phase expulsion from the molten surface.

Returning to the usually invoked athermal character, in view of the fact that part of the absorbed energy is nevertheless transformed in thermal load, "reduced thermal character" is a more appropriate description.[17,18] Especially concerning femtosecond irradiation of metallic surfaces, after the energy is deposited into the lattice, the processes related to phase transformation and material removal acquire a thermal character following the internal energy equilibration within the system.[19] The thermal character is present, therefore, even for irradiation with laser pulses with a duration considerably smaller than characteristic heat conduction time,[20] influencing the effectiveness of heat propagation.[21] In view of the still significant costs associated with the development and utilization of femtosecond sources, the question is if in the case of materials characterized by linear absorption (metals) advantages cannot be forecasted for laser pulses with longer durations. Consequently, the criteria for quality processing should be defined with respect to the efficiency of material removal, the smoothness of the residual structure, and the droplet content of the ablation products. In this work we are addressing from an experimental and a complementary theoretical perspective several issues related to the employment of fs and ps pulses for laser ablation of aluminum, and we discuss several consequences for material processing applications in optimized irradiation conditions. We concentrate on issues concerning energy transport and conversion, phase transformations in nonequilibrium conditions, culminating with particle emission. Apart from applications in la-

 

ser machining, the results presented here can be meaningful for a series of adjacent application areas, such as laser-assisted generation of nanoparticles, laser-induced breakdown spectroscopy, and pulse laser deposition. Stabilizing the input fluence to a regime characteristic to laser ablation and material processing, i.e., several times above the material removal threshold, we focus on factors determinant for optimizing energy coupling and for defining the kinetic properties and, respectively, the composition of the resulting plume. The issue of optimizing energy coupling in metallic materials is addressed by implementing advanced optimization algorithms in connection to laser pulse temporal modulation with a result in designing suitable irradiation sequences. Largely applied in femtochemistry, adaptive optimization techniques based on real-time pulse tailoring on ultrafast scales is an attractive technique to achieve control on laser-induced phenomena.[22–25] The attractiveness of these techniques is particularly prominent when prior knowledge on the interaction physics is not available and potential is foreseen in laser material processing applications. We intend to demonstrate that processes involving phase transitions can be guided by suitable energy delivery, and, therefore, particular thermodynamic states can be obtained, not by a brute energy force, but by optimally adapting optical excitation to the dynamics of phase succession and to the associated transient material properties. This way, efficient energy coupling and highly volatile states may be reached with minimal energy expenses and judicious adjustment of the energy flow.

The work is organized as follows. The experimental section presents the experimental concepts used in probing the energy content of the superficial layers by ion and neutral emission, followed by a discussion of the kinetic properties of the plume. The characteristics of the optimal irradiation are presented with respect to the ion emission efficiency. The theoretical section describes the physical rationale, and the main features of the numerical model provide insights into the hydrodynamic advance of the laser-excited matter, and discuss possible thermodynamic scenarios for material removal, while comparing swift femtosecond excitation with irradiation sequences acting on the timescale of the material motion. Emphasis is placed on early thermodynamic evolution and material motion, and on the responsible drive factors related to transient optical and nonequilibrium thermal properties. The discussion section compares the experimental and theoretical observations, analyzes various aspects of the energy coupling into the opaque materials, provides plausible explanations for the observed phenomena, and emphasizes consequences for laser-assisted material removal. The paper concludes by analyzing the relevance of the results in the context of ultrashort pulse laser interaction with metallic materials.

## II. EXPERIMENTAL SECTION

### A. Experimental setup

High purity (99%), mechanically polished aluminum (Al) metallic samples ($10\times10\times1$ mm$^3$) fixed in electrically-grounded holders were irradiated in vacuum conditions ($10^{-5}$ mbar) with 180 fs pulses from a near infrared 800 nm wavelength Ti:Sapphire oscillator-amplifier laser system delivering 0.6 mJ energy per pulse at a nominal repetition rate of 100 Hz. The laser system incorporates a closed-loop programmable pulse-shaping apparatus[26] and additional particle detection devices are attached to the irradiation system.[27]

The energy in the laser pulse was varied using calibrated neutral density filters. and a half-wave plate in combination with a thin film polarizer. Temporal pulse tailoring[26] was realized by dynamically altering the spectral phase of an incident bandwidth-limited laser pulse, which is spatially dispersed and reformed in a zero-dispersion unit that includes a 640-pixel liquid crystal (LC) modulator (Jenoptik) in the Fourier plane. The use of LC modulators in spectrally dispersed beams allows programmable spectral phase modulation, tailoring in turn the pulses to desired temporal shapes. The maximal shaping window allowed by the spectral resolution of the system is 22 ps. Our setup was used in the phase-only modulation scheme, thus keeping constant the energy in the pulse, which was then delivered at different rates. The optical modulator was inserted after the oscillator, the amplifier being seeded with the phase-modulated beam. Therefore, small energy variations determined by the discrete spectral phase modulation are minimized and the beam is regenerated energetically and spatially.[28,29] The temporal profile of the modulated sequence was measured by background-free second order cross-correlation with a non-modulated pulse deflected from the oscillator prior to phase modulation, and seeded in the amplifier 500 ps after the modulated pulse.

For ion recording, the *p*-polarized, spatially Gaussian laser beam was focused onto the Al sample at 45° incidence down to a spot of $\sim950$ $\mu$m$^2$. For recording neutral particles, the incidence angle was preset to 45°, while preserving the same focusing conditions. The positively charged ions were detected by a linear time-of-flight (TOF) mass spectrometer in a Wiley-McLaren configuration, with the detection axis normal to the sample surface. The emitted ions were allowed to drift for 65 mm in a field-free region, then extracted into the mass spectrometer with a pulsed electric field from a restricted region of 9 mm, and detected with a microsphere plate situated at a distance of 289 mm from the target. The extraction region is delimitated by two copper grids. Additional electrostatic voltages are placed on the particle path inside the spectrometer, having the role of temporally focusing the extracted particle beam upon arrival at the detector plane. The second role of the electrostatic optics is to eliminate particles arriving from the adjacent zones, allowing only particles from the extraction region to be transported to the detector. The pulsed voltage applied on the extraction grids at different delay times with respect to the laser pulse allows the construction of the ions' time-of-flight trace for a specific mass in a sequential manner. Consequently, the mass-resolved velocity distribution is retrieved at the position of the extraction region by applying the appropriate Jacobi factors. The variable extraction-field delay samples the expanding ablation plume temporally and the ion signal recorded for a given extraction time corresponds to a well-specified velocity of the ions. Details concerning the TOF mass spectrometry technique are given elsewhere.[30]

A similar experimental setup is used to monitor the neutral emission from the irradiated samples by using post-

ionization sources and repelling voltages for the primary ions. For the detection of neutrals, a deflecting field (1.5 kV) was used before the extraction region to remove the ions from the plume and to allow only the neutral particles entering the extraction region of the TOF spectrometer. A XeCl excimer laser at 308 nm and 10 ns pulse duration was used as a secondary ionization source for neutral Al ionization in the extraction region. Once charging occurs, the electrostatic voltages within the TOF spectrometer are guiding the ionized particles towards the charge detector. The ionization occurs via resonantly enhanced multiphotonic processes, and hence only Al-based neutral species and aggregates are measured. No other species or contaminants appear in the mass spectrometer. The UV laser beam was focused in the center of the extraction zone to a spot size of approximately 1 $mm^2$. The number of detected secondary ionized particles is proportional to the number of neutrals present in the extraction region within the XeCl pulse focal volume. The delay of the excimer laser pulse was controlled with respect to the short near-infrared pulse by using an electronic delay unit triggered by the incoming Ti:Sapphire laser pulse. The subsequent sampling of the neutral plume was used for constructing the velocity distribution for the neutral components. Since particles are detected from within a fixed spatial region (the same argumentation as for the ion measurements holds in this case, too), the velocity distribution is obtained by multiplying the detected number of particles at different delay times with the corresponding extraction time value.

An electromechanical shutter was used to control the irradiation dose, scaling the repetition rate down to 1 Hz, and releasing a controllable number of pulses in a single irradiation event. The number of selected consecutive pulses ($N$) was 10 for the ion detection part and 8 for neutral detection in our case, with 10 ms between the pulses in the irradiation run. The sample was translated between two subsequent irradiation sequences so that a fresh spot was illuminated at the beginning of each sequence. The $Al^+$ and $Al^0$ signals were recorded for the last pulse in the sequence, when the $O^+$ signature of the native oxide layer almost vanishes. This was used as a proof that the native oxide layer was practically removed prior to particle recording. The $O^+$ trace does not disappear completely but remains at a negligible level due to the following reason. The spatial Gaussian profile of the laser pulse allows the presence of the native oxide layer at the wings of the profile, where the energy density is too low to ablate efficiently, but this does not really contribute essentially to the measured TOF signal. At the same time, the 10 ms separation between consecutive pulses does not allow sufficient time to recover the surface with a fresh oxide layer of noticeable thickness with respect to the ablation rate. The number of pulses in the irradiation sequence was kept to a minimal value in order to avoid crater formation, ensuring at the same time a cleaner surface. In addition, all samples were cleaned in methanol before irradiation without other complementary preparation steps.

### B. Experimental results

Material removal from laser-irradiated metals is precluded by several steps that accommodate energy absorption. During illumination, the laser radiation is coupled to the electronic system in intraband transitions via inverse bremsstrahlung and the electronic system suffers a swift increase in its internal energy. This energy is transferred to the lattice on a timescale defined by the strength of the electron-phonon interactions (usually on ps range) and the material commences its series of thermodynamic transformations, culminating with material removal. Phase transformation proceeds by the thermodynamic collapse of the lattice towards a disordered state. The effective heating rates determine the temperature gain and overall losses, and have a decisive impact on the path the material will follow in the thermodynamic phase space.

#### *1. Optimized emission of charged particles*

We consider in the present case that emission efficiency for the particles generated following the laser-induced phase transitions is sensitive to the amount of energy density stored in different layers of the material. The subsequent evolution of the gas-phase particles may affect the surface thermodynamic conditions to a certain respect but will leave the volume excitation events largely unaffected. Moreover, the plume kinetic parameters and translational temperatures are developing in the same direction as the thermodynamic conditions at the vacuum-material interface. Consequently, in response to the optical excitation, the emissivity should depend on the laser energy delivery and relaxation rates. To prove this point, we have attempted to optimize (i.e., to maximize in our case) in a first run of experiments the ion yield emitted from the Al sample exposed to laser excitation, by varying the temporal shape of the incident laser pulse in a closed feedback optimization loop. The adaptive optimization loop includes the pulse tailoring unit that performs the programmable variation of the incoming temporal intensity envelope, providing at the same time the functional degree of freedom for the optimization procedure, and the ion detector which delivers the quantitative evaluation of the laser action. The task of optimization of energy coupling presents usually two conceptual aspects and it can be related to (i) a minimal threshold energy to trigger a specific laser-induced process, and (ii) the occurrence of a maximum throughput at a given constant incoming energy. Choosing the latter as an objective for the optimization procedure, we have selected the fast ion emission[31] as a qualitative probe for the amount of energy deposited in the superficial material layers at input fluences corresponding to laser ablation regimes.[32,33] To investigate a larger region of incoming fluences, two energetical domains were selected and defined with respect to the experimental ion emission threshold at short pulse durations ($F_{th} \simeq 0.15$ J/cm$^2$ average fluence, equivalent to a peak fluence of 0.3 J/cm$^2$); the low energy range at $3F_{th}$ and the high energy range at $5F_{th}$.

Laser-induced ion emission is used as a candidate for pulse tailoring experiments due to the benefit of a succession of phase transformations on a ps scale that may be regulated by the incoming radiation. The experimental system allows the detection of the quantity of ions emitted in a single laser pulse and characterized by a single velocity. The amplitude of the ion signal with a chosen velocity $v = 4.7 \times 10^4$ m/s,

corresponding to a fixed extraction delay time in the TOF mass spectrometer, serves as feedback for the optimization loop. The measured output of the ion yield is fed back into the iterative loop until an excitation sequence is found, able to generate the maximal experimental signal. The use of velocity windows adds flexibility to the process of manipulating the ion beam and allows the controlling of different portions of the velocity distribution. For the purpose of this paper, we have worked with a single velocity window in the high velocity range, where the efficiency of optimization is maximal. The optimization is performed using a self-learning evolutionary strategy that produces suitable spectral phase masks and programmable manipulation of the temporal laser pulse envelopes. The procedure starts from a set of arbitrary initial phase patterns applied on the optical modulator, which evolves through computer-designed genetic propagators. The Fourier-transformed pulse is part of this initial population most of the time. Results are ranked according to the generated magnitude of the ion yield, and the algorithm will suggest in the next step an improved collection of solutions, searching the multidimensional space similarly to biological evolution. In other words, assessing the signal, the algorithm selects the phase patterns that have produced the highest ion yield during one generation, and, by mimicking genetic evolution, it iteratively proposes solutions based on the "survival of the fittest" selection until convergence is achieved. Due to the intrinsic genetic evolution, evolutionary algorithms are robust against experimental noise and improvements are obtained even for complex topologies of the solution space or reduced excitation selectivity. Details about global optimization methods can be found elsewhere.[34]

The optimal irradiation sequence that achieves the highest ion signal is obtained by setting the algorithm parameters for a fast and smooth convergence. The results in the ion velocity distribution after irradiation with single short pulses (SP) and optimal pulses (OP) are given in Fig. 1 for two fluence levels, approximately three times [Fig. 1(a)] and five times [Fig. 1(b)] above the ion emission threshold. The broad velocity envelope suggests the presence of several stream velocity components corresponding to different stages of removal, i.e., different moments of ejection and depths of origin, as a function of the locally stored energy density. Since the emission process may require a finite amount of time, with variable conditions at the vacuum-solid interface, the distribution of the ejected particles includes a mixture of different drift velocities and translational temperatures,[35] notwithstanding translational equilibration regions and additional mutual Coulombic interactions in the gas phase. The SP graphs show a velocity distribution peaked around $1-1.5\times10^4$ m/s, depending on the input fluence, with a low magnitude velocity shoulder at higher velocity values. Responding to the character of optical excitation, the ion velocity distribution resulting from irradiation with the optimal pulse (OP) shows a boost of the high velocity ion wing as compared to the short pulse result. The tendency of accelerating ions is present in both fluence regimes and the high velocity region is most sensitive to the character of irradiation. It is expected that the choice of different velocity windows may affect the result of the optimization, since the ejected particles may correspond to different times and regions of emission, but, in the view of the overall increase in the ion yield, we expect this influence to be minimal. The temporal intensity envelopes (Fig. 2) corresponding to several optimal sequences (OP1, OP2) found by the algorithm show a distribution of intensity spread on a ps time scale. Despite the noise imposed by the randomness of the initial pattern population on the optical modulator and the discrete nature of the liquid crystal array, the temporal stretching of the optimal pulse suggests that the mechanisms of control are connected to the synchronization with the hydrodynamic material expansion during the energy deposition process. While using most efficiently the absorption channels to maximize

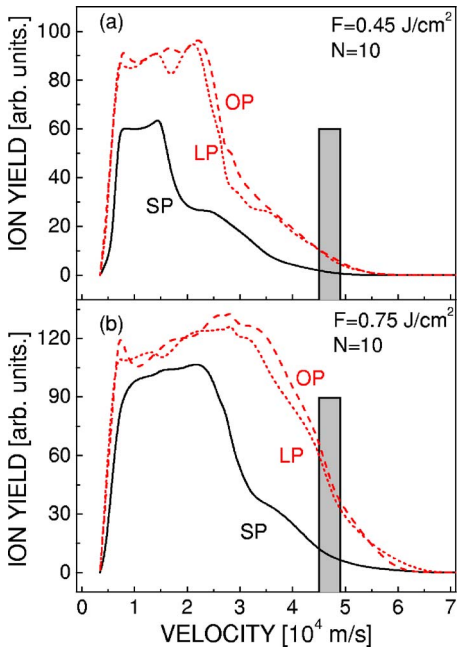


FIG. 1. (Color online) Velocity distributions of Al ions emitted from aluminum targets irradiated with short (SP), optimized (OP), and long (LP) pulses at two different input average fluence levels. (a) F=0.45 J/cm$^2$, approximately $3F_{th}$. (b) F=0.75 J/cm$^2$, approximately $5F_{th}$. The optimization velocity window is also marked in the figure.

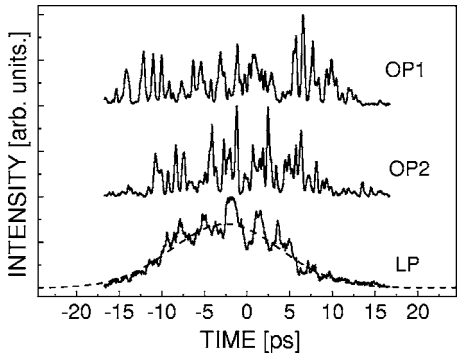


FIG. 2. Normalized temporal optimal intensity profiles at similar energies (the two upper OP1 and OP2 curves) and the long laser pulse (LP) envelopes used in the experiment and, later, in the simulation procedure (bottom solid and dashed curves). The OP1 curve is used to illustrate the laser action under the optimal conditions.

the deposited energy, the optical properties of the sample are dynamically changed to accommodate optimally the incoming energy rate. In other words, the input energy has adaptively adjusted to the dynamic properties of the sample and rebalanced in time in a synergetic manner to obtain an efficient thermodynamic path towards the generation of a high ion yield. Stimulated by the optimal pulse stretching on a ps time scale, we have investigated also the effect of a longer laser pulse (LP) of 15 ps full width at half maximum (FWHM) [Fig. 2 (bottom)] and observed the same type of ion velocity distribution as in the OP case. This is not surprising in the view of the fact that the absorption mechanism in aluminum is linear in a first approximation. In fact, the particular shape does not play a significant role as long as the energy delivery is synchronized with the relevant transformations and heat dissipation effects are not significant. In addition, since it is reasonable to assume that thermal aspects are dominant in the characteristics of ion ejection, the solution landscape has slow-varying envelopes for the optimal points. Moreover, the selectivity of excitation is reduced due to the involvement of the conduction band electrons in regulating the energy transfer and to the rapid dephasing of the electronic continuum states. Therefore, particular pulse forms stretched on this time scale will deliver more or less the same result as long as the heating rate is high enough to overcome losses by diffusion. This allows for a large selection of optimal solutions to be generated and the creation relays on the most efficient path for energy transfer from the laser source to the material. Nevertheless, deviations may originate from instantaneous variations in material properties. As will be shown below, the drive factor for the observed ion acceleration is the succession of matter transformations occurring under the laser pulse envelope, leading to material advance and density variations. The substantial increase in the amount of high velocity, thermally generated ions indicates that the decomposing matter has achieved a significant temperature, with a noticeable component in the ionized state. The practically volumetric decomposition of matter and the eventual appearance of discontinuity layers to attain collisional translation equilibrium will subsequently organize the particle flow while amplifying these effects. The optimal pulse is therefore a balance between elevated heating rates and the characteristic time for the variation of the optical properties upon material transformations. The latter is defined to a certain extent by the strength of carrier-phonon interactions and by subsequently triggered expansion of the hot material. Pulses much longer that the heat conduction time,[20] extending on a ns scale at these fluence levels, are giving little signal if at all.

The augmentation in the high velocity ion yield for the optimal pulse can be therefore related to a better coupling of energy in the expanding matter. As it will be demonstrated in the following, this increased coupling is not due to a change in the optical properties of aluminum during the solid-to-liquid transition as it was previously demonstrated for semiconductors.[31] Actually, the complex refractive indices of both solid and liquid phases are quite similar when probed at 800 nm. The reason is associated with the density gradient that forms above the surface, which becomes quasitransparent upon expansion, leading to increased energy deposition

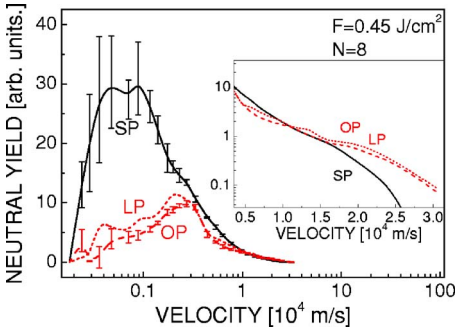


FIG. 3. (Color online) Velocity distributions of neutral ejecta emitted from aluminum targets irradiated with short (SP), optimized (OP), and long (LP) pulses. The inset shows a blowup of the high velocity range.

inside the material and exposing the bulk part to the laser radiation.[36,37] This particular fact, as will be seen in the following theoretical section, has consequences also on the resultant liquid layer that forms upon energy relaxation. The higher heating efficiency for the long pulse sequence will favor the gas-phase transition and this translates into a reduction in particulates ejection. It is worth mentioning that the SP always delivers the smallest yield in the high velocity region within the investigated time windows and fluence levels above a value which is roughly two times the ion emission threshold. On the contrary, in the close vicinity of the threshold, the short pulse provides the most visible signal and the SP threshold has the lowest value.

By increasing the input fluence, the gap between the SP and the OP or LP ion spectra goes slightly down and the particle velocity distributions become similar at a fluence superior to approximately 2.0 J/cm$^2$.

### *2. Emission of neutral particles*

Having observed the ion acceleration, other ablation products were investigated to verify if the same observations operate. We have applied the same irradiation sequences (SP, OP, LP) that optimize the fast ion emission, and we have monitored the emission of neutral Al ejecta under the laser action via secondary ionization mass spectrometry. Since secondary ionization is used to generate detectable ions in the mass spectrometer from originally neutral particles, several assumptions have to be made on the nature of the primary products. The SP distribution (Fig. 3) shows a slow beam, with a peak in the $10^3$ m/s velocity range. Two regions can be observed. The high velocity edge is characterized by low signal fluctuations. This region corresponds to a genuine secondary ionization of atomic Al in the gas phase. A second region of high fluctuations can be noticed on the tail of the distribution, with velocities in the range of several $10^2$ m/s. Based on the strong fluctuations of the signal in the low velocity range, this can be attributed to the occurrence of small nanodroplets in the region of secondary ionization. Actually, no precise assumptions on the size can be made only based on the TOF information, but, taking into account the corresponding velocity, it is reasonable to propose particle dimensions on the nanoscale. The appearance of high density

material regions within the ionization region in a noncontinuous manner should lead, as observed, to high signal variations. Due to reduced free-flight region, the TOF spectrometer is not sensitive enough to cluster detection. Upon irradiation with the picosecond pulse, the neutral distribution shows a significant decrease of the low energy tail (Fig. 3), while a slight acceleration of the OP/LP-generated species can be noticed on the leading edge (see inset in Fig. 3 which shows a blowup of the high velocity range).

Two conclusions are evident at this point. The ps irradiation leads to a significant acceleration of the ionic component. The distribution of secondary ionized particles shows merely a reduction of the low velocity yield that originates from nanodroplets and clusters, and little acceleration is observed. The behavior can be explained by considering the amount of energy stored in the superficial layers and shows that short exposure is not always the most efficient way to couple energy in the system, despite the fact that illumination and heat conduction are temporally separated. If the ion acceleration, respectively, the increase in the high velocity ion yield is related to a significant augmentation of surface temperature following optimized absorption, this is subsequently pursued by an increase in the ionic weight in the plume on the expense of the neutral component. Additionally, the preferential transition to gas-phase states for the picosecond pulse will lower the probability to liberate material in the form of liquid droplets and clusters.

The observations related to the fact that the stored amount of energy depends on the delivery rate will be used below to extract information on the thermodynamic series of transformations in the excited material in the early times of energy relaxation.

## III. THEORETICAL DESCRIPTION

In order to understand the complex sequence of material transformations under the laser action, we have performed numerical simulations of the hydrodynamic advance of the excited matter. Modeling laser-matter interactions is a current challenge, requiring multidisciplinarity and the interconnection of different physics fields, including optics, heat transfer, fluid dynamics, and phase transitions in nonequilibrium frames. Among different models that treat the interaction between ultrafast laser light and metallic targets at moderate intensities and provide scenarios of material ejection,[38–42] the hydrodynamic approach employing tabulated Bushmann-Lomonosov-Fortov multiphase equations of state[43] (EOS) addresses reasonably well the complexity of the problem, and has the potential to reveal plausible evolution paths for the excited matter, that also have relevance for improving the laser interaction process. The question we have tried to answer refers to the energy conversion in the excited material and, subsequently, to the form in which material is being removed after the laser excitation, together with its kinetic properties. The issues of primary concern for these calculations follow energy transport and conservation arguments, and are related to the energy deposited in different superficial layers and to the global amount of energy stored within the material. These have consequences for the velocity of surface expansion in the early moments, where fluid assumptions still hold, and for the amount of excess energy in the first nanometers of matter, driving very specific thermodynamical transformations. They have, as well, consequences for the significance and the lifetime of the liquid phase. The superficial temperature determines, though indirectly, the kinetics of particle emission and, to a certain extent, the ionization degree, while the transient liquid layer controls the direct ejection of nanodroplets.[44–46] Although we acknowledge alternative mechanisms for the formation of aggregates in the gas phase which require the involvement of nucleation theories with a complexity beyond the scope of this paper, we do not refer here to nanosized complexes formed by coalescence of matter in the plasma plume.[47] Additionally, phase decomposition is suggested as playing a complementary role, but the situation is not detailed. We focus here on droplet emission directly from the liquid phase. At the same time, the gas dynamics of the plasma[48–50] is not discussed. This seems to be an oversimplification at first glance, but the arguments provided in the text point out the primary thermodynamic phase transformations following laser energy conversion as the controlling factor for the observed behavior. Nevertheless, occasionally, possible influences of the gas-phase effects are noted. The modeling approach[51] is based on a 1D-Lagrangian hydrodynamic code (ESTHER) developed at the Commissariat à l'Energie Atomique, France, that includes features of the two-temperature model (TTM) to account for the initial laser-induced nonequilibrium between the lattice and the electronic system.[38,52–55] The Lagrangian approach permits an accurate description of the primary thermomechnical transformation in the excited material. The Helmholtz wave equation for optical propagation is used in tracking down the energy flow at 800 nm and *p* polarization, and this allows the determination of the electromagnetic field through the entire region illuminated by the laser pulse. The deposited energy is then deduced using the Joule-Lenz law.[56] The material data used in the numerical simulations and a detailed description of the calculation steps are given in Ref. 51 and in the references therein. To facilitate understanding, the main model assumptions are indicated below.

As the energy absorption in the electronic system proceeds by inverse bremsstrahlung, the cross section of free-electron heating and, as a consequence, the efficiency of absorption of electromagnetic radiation, depends on the carrier transport properties and, implicitly, on the temperature and the density of the material. The degree of nonequilibrium established between hot electrons and the initially cold lattice on the irradiation time scale is an additional factor that determines the electronic transport and, consequently, the absorption rates.[57–59] On estimating the profiles of energy deposition in the electronic system by the Helmholtz formalism for optical propagation, analytical solutions in the case of homogeneous media are used as boundary conditions to numerically integrate the propagation equation in the nonuniform regions crossed by the laser beam. To estimate correctly the probability of absorption, the local optical properties in every calculation cell are calculated using the high frequency (ac) electrical conductivity for each temporal step in the calculations. The dc component of the conductivity value is

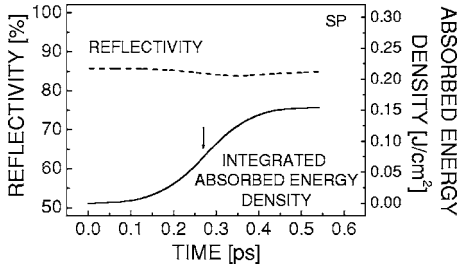


FIG. 4. Simulation of the instantaneous reflectivity values and of the integrated absorbed energy density as a function of time for a 180 fs laser pulse (SP) exciting the aluminum sample at 800 nm wavelength. The incident fluence value is 1 J/cm$^2$. The arrow indicates the maximum of the laser pulse.

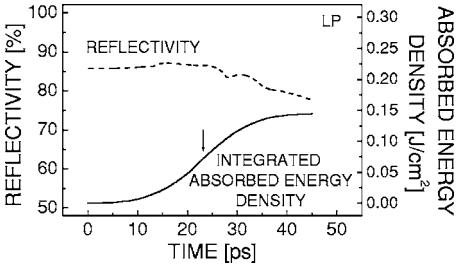


FIG. 5. Simulation of the instantaneous reflectivity values and of the integrated absorbed energy density as a function of time for a 15 ps laser pulse (LP) exciting the Al sample at 800 nm wavelength. The incident fluence value is 1 J/cm$^2$. The arrow indicates the maximum of the laser pulse.

tabulated for a wide range of temperatures and densities.[60] Note that at solid density and at 800 nm irradiation wavelength, the standard value of the complex index of refraction is used; $n=2.8+8.45i$.[61] The ac conductivity is described by the Drude formalism[62] that regulates with good accuracy[63] the influence of the electronic density and collision frequency. The initial collision frequency is chosen to match the optical properties in standard conditions. Electrical conductivity depends both on the electronic and ionic collision rates, and the evolution is consequently dictated by the degree of nonequilibrium controlled by the TTM. The thermal conductivity follows a similar behavior and shows a smooth transition when passing from the solid to the liquid state. Part of the incoming energy is locally converted into thermal energy by Joule heating and the other part is reflected from the interface. The power dissipated in the unit volume is therefore $\mathcal{P}_{Abs}(z,t)=\sigma(z,t)\mathcal{E}^2(z,t)$, where $\sigma(z,t)$ is the local electrical conductivity and $\mathcal{E}(z,t)$ the amplitude of the electric field at the $z$ location. In our calculation, the thickness of the material is sufficiently high relative to the skin depth to ensure zero transmission at the rear side of the sample. The beginning of the laser pulse sets the initial time for the interaction.

To identify the drive factors for the observed ion acceleration and reduction in droplet emission, we have performed simulations in different conditions of irradiation. The maximum simulation window is 5 ns, that puts an end to the calculation before global thermal relaxation occurs. The incidence angle for the incoming radiation in the simulation run is the same as for the experimental ion detection part (24°). The first results are derived by comparing the energy absorbed in aluminum for SP and LP sequences at the same input fluence, 1 J/cm$^2$. This value is about two times higher than the calculated ablation threshold for the short pulse ($F_{th}=0.45$ J/cm$^2$) for reasons that will be given in Sec. III A. In the present context, the threshold for macroscopic material removal in gas phase is defined by the transformation in vapor phase of the first nm of material in the thermodynamic conditions established by the multiphase EOS.

### A. Transient optical properties

The time-integrated energy density absorbed during the pulse exposure and the temporal behavior of the reflectivity are presented in Figs. 4 and 5 for two relevant pulse shapes, SP and LP, respectively. The reflectivity graph $\mathcal{R}(t)$ shows the instantaneous reflectivity values while the absorbed energy per surface unit is integrated in time and reflects the history of absorption. These two quantities are interconnected by energy conservation arguments and describe in a global manner the complex optical properties. The absorbed energy density $\mathcal{F}$ in a one-dimensional medium of a given thickness is defined therefore by:

$$\mathcal{F}=\int_0^L\int_0^t \mathcal{P}_{Abs}(z,\tau)dzd\tau=\left[1-\frac{\int_0^t \mathcal{R}(\tau)|\mathcal{E}_{z<0}(\tau)|^2d\tau}{\int_0^t |\mathcal{E}_{z<0}(\tau)|^2d\tau}\right]F_{inc}, \quad (1)$$

where $F_{inc}$ is the incident fluence and $\mathcal{E}_{z<0}(t)$ is the incident electric field amplitude. $L$ is the geometrical thickness of the sample ($L=10$ $\mu$m).

In the case of short, sub-ps irradiation, the optical response of the excited material appears later in the laser pulse and Fig. 4 displays a weak change in reflectivity during the SP action. The reflectivity value remains close to the standard value of 85.7% at 800 nm for most of the exposure time. The final decrease is due to an augmentation in the electron-electron collision rate associated to an increase in temperature for the electron gas confined to the solid density material. Interband transition effects at 800 nm (Ref. 64) are negligible at this relatively low fluence and, therefore, do not contribute to the optical properties. Nevertheless, they are accounted for in the form suggested by Ref. 65. The integrated absorbed energy per surface unit reaches 0.154 J/cm$^2$ at the end of the laser pulse and represents 15.4% of the incident energy.

The situation changes for longer pulse durations. Figure 5 shows a more pronounced change in reflectivity as a function of time for the longer pulse. The reason is connected to the onset of hydrodynamic effects during laser exposure and to the appearance of a density gradient in front of the surface. In the first picoseconds, reflectivity increases following a rise in the extinction coefficient due to laser heating and a subsequent gain in ionic temperature.[66,67] The decrease in reflectivity which starts around 25 ps is due to surface expansion

which coerces the material density to decrease in the absorbing region. In nonequilibrium regimes, both electron-electron and electron-ion collisions are determinant factors for light absorption (in view of elevated electron temperatures) and the dependence of the transport properties on density and temperature is particularly complex. However, for the long pulse, the electron-ion relaxation time is shorter than the pulse duration and the electron-ion collision rate driven by the ionic temperature is the control knob for the absorption rates. Consequently, the electrical conductivity decreases with density but increases steadily with the ionic heating. Electromagnetic energy is gradually transformed into thermal energy, hydrodynamic surface motion commences during the pulse irradiation, and, as a result, electronic density decreases in the absorption region. The increase in the electron density gradient scale length is responsible for the reflectivity decrease with time. The integrated absorbed energy per surface unit reaches 0.145 J/cm$^2$ representing 14.5% of the incident energy and is just below the subpicosecond value at this particular fluence of 1 J/cm$^2$. It will be shown below that this fluence value represents a superior limit of the energy window where ultrashort pulse absorption is still the most effective process of energy deposition.

A summary of the simulation runs performed at input fluences below and above 1 J/cm$^2$ indicates that, for pulses with a fluence lower than 1 J/cm$^2$ the absorbed energy is more important for the 180 fs laser pulse than for the 15 ps laser pulse. The absorbed energy becomes equal for both cases for fluences around 1.1 J/cm$^2$ and this is merely a consequence of the fact that decreased reflectivity offers the premises for better absorption. This value plays the role of an efficiency junction. For fluences above 1.1 J/cm$^2$, the energy stored in the target during the ps irradiation significantly surpasses the energy deposited in the SP case and creates the condition for an additional heat load into the superficial layers. In other words, the observed reflectivity decrease implies that the energy is absorbed in a thicker low-energy-density layer. The integrated absorption augments due to the additional boost in the characteristic scale length, even though the absorbed energy density in the first subsurface layer decreases. To observe in greater detail the thermodynamic conditions at this crossing point, we have concentrated mainly on simulations at 1 J/cm$^2$, i.e., two times above the short pulse material removal threshold, while the other fluence ranges are treated in a more concise manner for comparison purposes. Actually, even though the absorbed energy is similar at this fluence, notable differences between short and long pulse irradiation are clearly observed in their thermodynamic evolution. Since the fluence values are not one-to-one translatable between experiment and theory, numerical simulations are made also at 0.5 J/cm$^2$ and 2 J/cm$^2$ with the purpose of enlarging the perspective upon the variety of phenomena occurring within the excited sample. The situation corresponding to the experimental observations will be addressed briefly as well. Note that for comparing the experimental and the theoretical results, the material removal threshold is used as a relative reference, and the irradiation regime is situated in both cases at more than three times the respective threshold (0.15 J/cm$^2$ for the experimental part, and 0.45 J/cm$^2$ for the simulation part, respectively). This being said, the average experimental fluence of 0.45 J/cm$^2$ corresponds to a theoretical input fluence of approximately 1.5 J/cm$^2$, and an experimental input fluence of 0.75 J/cm$^2$ matches a simulated fluence of 2.2 J/cm$^2$.

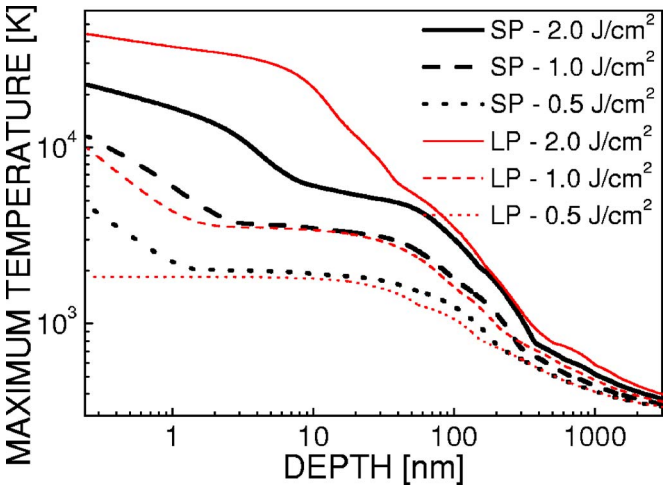


FIG. 6. (Color online) Maximum transient ionic temperature as a function of the initial, unperturbed solid depth for different fluences and for the two sets of laser pulses. The critical temperature is 6300 K.

It is also noteworthy to observe that, in the experiment, the incoming laser intensity has a spatial Gaussian distribution and the reported fluence is averaged on the spot size. On the contrary, in the 1D calculations presented here, the intensity distribution within the laser spot is uniform and the simulations are performed in conditions of constant energy distribution. For this reason as well, simulations have been realized for different fluence values. This facilitates a better comparison with the experiment and suggests the thermodynamic processes that may occur in different regions illuminated by the laser spot. Obviously, the numerical procedure presented here has limitations in reproducing a realistic nonuniform irradiation because no transversal gradients are considered in our calculations. In the absence of a nucleation formalism, the kinetics of the phase transition is not pictured. At the same time, the 3D expansion of the plume is not captured by the simulation. However, simulation under fluence conditions below and above the experimental peak fluence can bring indispensable insights into the processes occurring during and after the interaction.

### B. Conditions for reaching supercritical thermodynamic states

Since temperature is one of the main parameters defining the thermodynamic state, we have investigated the temperature achieved in different layers below the surface in the course of evolution. Figure 6 shows the profile of the maximum temperature reached within the material body for an aluminum sample irradiated by 180 fs (thick lines) and 15 ps (thin lines) pulses. The position of the layers correspond to the initially unperturbed solid and no information regarding the state of aggregation for the different regions is provided at this point. Situations corresponding to three different laser fluences are displayed. The lowest value, at 0.5 J/cm$^2$, rep-

resented by the dotted curve, corresponds to the outer ring of the Gaussian pulse of 1 J/cm$^2$ average fluence. The maximum temperature reached due to the subpicosecond pulse is higher than the temperature achieved under picosecond irradiation since the absorbed energy density is more elevated for short pulse exposure at this particular fluence. Nevertheless, in both cases no supercritical state is reached at the surface of the sample. For 1 J/cm$^2$ (dashed curve) similar observations can be made, and a very thin layer, less than 1 nm, surpasses the critical temperature (approximately 6300 K for aluminum). For a higher fluence (2 J/cm$^2$), depicted with solid lines in the graph, the LP absorbs more energy than the short pulse and a thicker layer of material has a maximal temperature beyond the critical value and superior to the SP value. Moreover, less energy is consumed in kinetic expansion for the LP case and the major part of electromagnetic energy is converted into thermal energy, as compared to preferential conversion in mechanical shock energy for the SP pulse. At this fluence, the maximum thickness of the supercritical fluid reaches 5 nm for the SP and 35 nm for the LP sequence. This difference is mainly due to the distinct optical properties which depend strongly on the matter expansion during irradiation. More explicitly, for the LP pulse, the increase in the electronic density gradient scale length drives the evolution of the optical properties, whereas for the SP pulse, even though the transport coefficients are strongly affected by electronic and ionic temperature gain, the electronic density remains equal to solid density during irradiation. Thus, the hot electronic layer produced by absorption is thicker for the LP pulse, which results, in turn, in producing supercritical states within a wider spatial region. Additionally, high electron temperatures for the SP induces a stronger electron mobility promoting the electronic heat conduction process. This results in reducing surface temperature. However, the change in optical properties upon density variations is expected to affect more efficiently the distribution rate of the deposited energy.

In the regime considered, with an ionic temperature situated below the first ionization level, the electrical conductivity decreases when temperature augments and the ionization rate decreases with density. The density dependence of conductivity is quite complex and, at a typical temperature of 1 eV, the conductivity decreases for density values between solid density $\rho_0$ and $10^{-2}\rho_0$, and increases for lower density down to $10^{-5}\rho_0$.[60] These spatiotemporal variations of the transport properties prepare the conditions for locally enhancing the energy absorption and, implicitly, drive high temperature levels, being an effective way to reach supercritical states. On the assumption that a correlation exists between supercritical states and fast ion production (note that the description based on equilibrium EOS cannot properly describe the superheating of unmixed states of aggregation), it appears that the rate of ion emission is clearly enhanced for LP at the higher fluence levels, as was seen in Fig. 1, driven by an excess of energy that offsets the intermolecular potential within the fluid. In this situation, the latent heat of vaporization decreases significantly, the kinetic energy of the atoms in the condensed phase becomes comparable to their binding energy, and the hot fluid may decompose to atomic gas-phase species without involving nucleation.[68] The atomized fluid can rapidly expand, ensuring high kinetic energies for the emitted species after translational equilibration in their flight path. Nevertheless, as usual in ablation experiments, different regions in the sample may achieve different temperatures, so they will follow accordingly a wider range of thermodynamic paths, some of them including nucleation of gas bubbles at various rates according to the superheating degree in the mixed-phase region, with the respective particles being emitted at different moments.

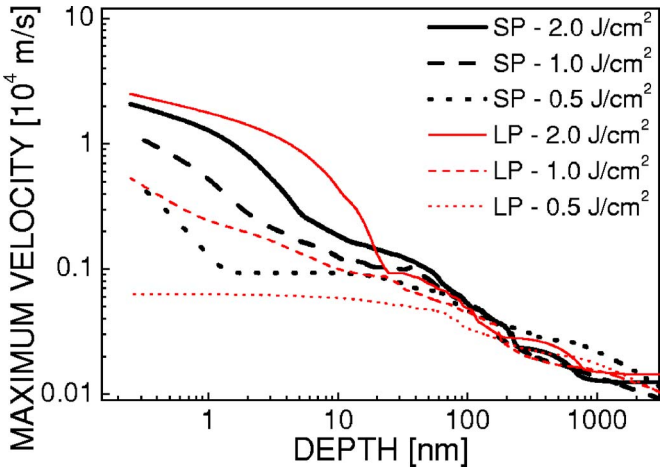


FIG. 7. (Color online) Maximum velocity of different expanding layers as a function of initial, unperturbed solid depth for different fluences and for the two sets of laser pulses, SP and LP.

The increase in temperature also has consequences for the impulsivity of the hydrodynamic expansion. The corresponding maximal velocities of various layers originating from different depth coordinates from the initially unperturbed solid is presented in Fig. 7. The figure delivers a perspective on the kinetic consequences of strong heating and shows the progressive acceleration of the LP-irradiated layers with increasing fluence as a consequence of the more effective temperature gain.

### C. Density behavior and liquid droplet ejection

Further insights are derived from investigations of the aggregational state of the excited layers at different moments during the material motion. Probing the density of the different layers upon expansion will provide answers to issues related to which part of the material participates to the ablation process. Figure 8 displays the transient density profile for a short pulse of 1 J/cm$^2$ scaled to the initial depth inside the metal. The density profile is presented for three relevant moments: thermal electron-ion equilibration (12 ps), onset of ablation (25 ps), and relaxation (5 ns). The representation is done with respect to the initial localization of the cells. The expansion of the individual cells is neglected in the graphic representation and the cells were restricted to initial dimension for all three moments of description. The scaling, occurring as if the spatial evolution was frozen, was made in order to fit different profiles to the same dimensional scale and to concentrate on the local material state. This approach permits us to follow the history of transformation in specific regions

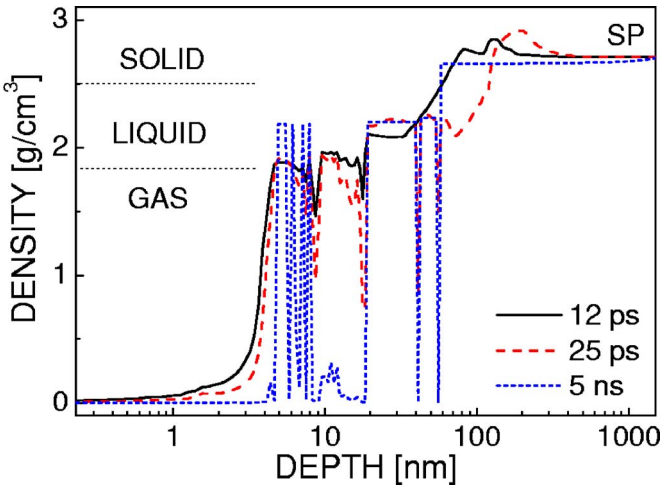


FIG. 8. (Color online) Density profiles at three different moments during the simulation of a 180 fs laser pulse interaction with aluminum. The solid-liquid and liquid-gas borders marked on the left side of the figure are an approximate indication of the respective transitions. The incident fluence is 1 J/cm$^2$.

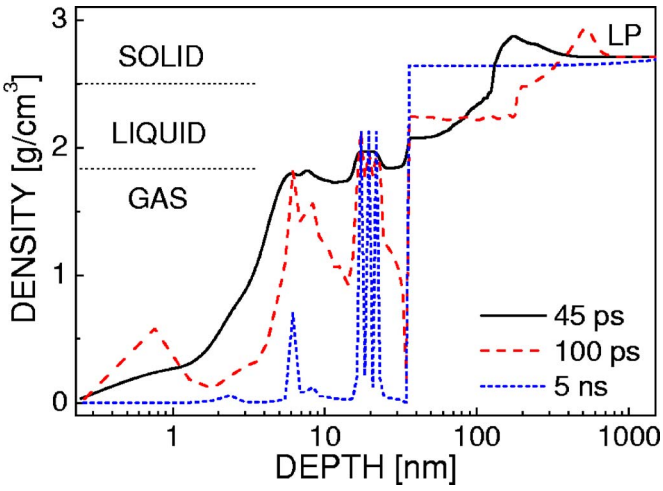


FIG. 9. (Color online) Density profiles at three different moments during the simulation of a 15 ps laser pulse interaction time with aluminum. The solid-liquid and liquid-gas borders marked on the left side of the figure are an approximate indication of the respective transitions. The incident fluence is 1 J/cm$^2$.

within the material, characterized by an initial depth and its own particular evolution. Consequently, the graph presents local material densities and the corresponding aggregation state reached at each calculation cell. The density limits marked in the figure and corresponding to different states of aggregation are only indicative, since the actual border depends on specific pressure and temperature conditions. The electronic-vibrational thermalization is already completed at $t=12$ ps and the solid curve shows the corresponding aluminum density in the laser-affected region. At the surface, only 4 nm of material is in the vapor phase and a region of approximately 30 nm of metal is pushed into a well-defined liquid phase. In deeper regions, the density gradient is smooth at this time and the solid-liquid interface is not clearly defined. The dashed curve represents the density profile at 25 ps, when the solid-liquid separation begins to appear at a depth of 56 nm. The thickness of the superficial region which suffered transformation to the gas-phase has not changed, but a liquid-gas mixture seems to break away from the liquid at 18 nm. The curve presents a plateau between 20 nm and the solid-liquid interface at 56 nm. The dotted curve corresponds to the density reached at the end of the simulation, at 5 ns. At this stage, the three aggregational states of matter are clearly distinguishable. The first one corresponds to vaporization occurring in the first nanometers below the surface. A liquid-gas mixture still exists in the first 10 nanometers, with regions at liquid density present as singularities, and the approximately first 18 nm of aluminum will most probably evolve as an ideal or ionized gas, if the transition is too fast for nucleating the vapor phase on this time scale.[68] The possibility of nucleating vapor nuclei in the liquid phase is mentioned briefly in Sec. IV where the duration of the passage through the metastable/unstable region is evaluated. The second state (the next 36 nm) corresponds to a liquid layer which survives a long time after the onset of heating and cooling caused by hydrodynamic motion and heat diffusion. It is limited by a very localized density collapse that suggests a spatial confinement. The last state is represented by the condensed state for the inner part of the material which returns to the solid density $\rho_0=2.7$ g/cm$^3$. For the SP case, both gas and liquid droplets contribute to the ablated matter and define the removal depth down to a penetration depth of 56 nm. In fact, the solid-vapor interface observed at 56 nm corresponds to a localized gas expansion which could be interpreted as a fracture occurring inside the liquid. The expanding fluid and the condensed substrate are then disjointed at this point. Consequently, the SP plume would be dominantly constituted by gas and liquid droplets. The droplet appearance on a tens of ps scale was previously validated by time-resolved imaging of laser excited surfaces.[69] As seen in the figure, the material undergoes a gas transition within a depth of 18 nm, while, deeper, several liquid droplets form, which will be subsequently ejected. Some uncertainties reside with the liquid part that may return to the solid phase, due to the absence of information on the cohesion properties of the liquid.

The density profile induced by a LP sequence of 1 J/cm$^2$ is depicted in Fig. 9 for three different moments during and after the interaction. The solid curve represents the density at the end of the laser pulse, at 45 ps, when it is considered that the electron-ion nonequilibrium does not exist anymore. At this time, the vaporization takes place for approximately 5 nm under the surface and around 100 nm are affected by liquefaction. The dashed curve corresponding to the density at $t=100$ ps shows a density collapse at 34 nm. The density associated to the deeper layers of matter shows a plateau characteristic of a liquid region down to a depth of 180 nm. This result indicates that the solid-liquid transformation is more extended in depth for the LP case as it was in the former case. The material region situated in front of the density fall can be regarded as a liquid-gas mixture, and the density is mainly below the liquid value. From the dotted curve representing the density profile at 5 ns when the simulation stopped, we clearly see that the mixture evolves pref

erentially to become a gas and the location of the density collapse has not changed. Contrary to the SP case, the liquid layer does not survive long enough to pursue a gas-phase transition path afterwards or to evolve as such by its own means, and resolidification occurs for LP on this time scale. As a consequence, an abrupt density gradient stands out at 36 nm and marks the solid-gas interface. Almost no liquid appears to be ejected in this case, the liquid layer returns preferentially to the solid state, and vaporization is the major material removal process predicted by the simulation. Two more consequences can be put forward for the LP case as compared to SP irradiation at this particular fluence. The ablation rate[51,70] is lower for the temporally stretched pulse whereas the layer of the resolidified liquid is thicker, contributing to the formation of a considerable amount of recast layer around the laser-induced crater.[71] Together with the preferential transformation to gas-phase, these aspects define the characteristics of the LP irradiation. The ablation rate grows rapidly with the input fluence, surpassing the SP rate at a fluence superior to 1.5 J/cm$^2$.

## IV. DISCUSSION

While trying to get to the roots of the physical events, further insights are gathered from interrelated ionic temperature and density estimations for the different states accomplished during expansion. Figures 10 and 11 display the correlated evolution of the thermodynamic properties of the metal in a density-temperature ($\rho$-$T$) diagram for both subpicosecond (180 fs) and longer (15 ps) pulses. The thermodynamic paths of chosen cells (reference equilibration time is marked in the figure to pinpoint major steps in the temporal evolution) are drawn in these diagrams, corresponding to an irradiation fluence of 1 J/cm$^2$. It was seen before by comparing the SP and the LP sequences that heat diffusion and hydrodynamic processes perform differently in response to the optical excitation, and their relative balance induces singular behaviors in both cases. The analysis of the corresponding ablation mechanisms estimates a high probability of droplet generation and ejection in the short pulse case and a considerably lower ejection rate for the LP case. The ($\rho$-$T$) thermodynamic paths are now compared in the short pulse (Figs. 10) and the long pulse (Figs. 11) situations to further distinguish between the particularities of material ejection in both regimes.

The first cell describes the outermost region at the surface of the bulk material (solid line), the very first layer (0.25 nm coordinate at the cell center). For both cases, SP and LP, a maximal overcritical temperature around 10 000 K is reached at the surface on the time scale of electron-ion relaxation in the first monolayers. Under the heat load produced by local absorption of electromagnetic radiation, the superficial part of the metal suffers fast and somehow exotic solid-liquid and liquid-gas transitions, [72] using the expansion energy to fuel its evolution.

Concentrating on the subsurface regions, for SP, three behavioral paths are followed by the excited matter: gas formation, liquid confinement, and melting resolidification. The first path, corresponding to the liquid-gas transformation, occurs for each cell localized between the surface and a limit corresponding to 18 nm inside the target (with the exception of a rather unusual trajectory of the first surface cell at 0.25 nm). The trajectory of this particular model cell at 18 nm (dashed thin curve), that serves as an example for the region between 0.25 nm and itself, is presented in Fig. 10(a). For cells below this depth, no fall of density occurs during the 500 ps following irradiation and the region remains liquid during the simulation time scale except for particular cells with singular behavior such as the deeper ones seen in Fig. 8, situated at 41.3 nm and 56 nm below the surface. The 41.3 nm fallout (the next cell after the still liquid one at 41 nm) in Fig. 8 is apparently an artifact of the simulation procedures since it is not stable against the cell size and simulation conditions, while the density drop at 56 nm appears to be a genuine thermodynamic feature determined by the evolution of the system. In establishing the physical authenticity of the features related to sudden density variations, we have used a criterion based on the stability of the numerical scheme against the simulation conditions (e.g., spatial and temporal sampling rates). At the same time, the passage through the instability region (crossing spinodal), though it follows in reality unpredictable states,[73] is in our case artifi-

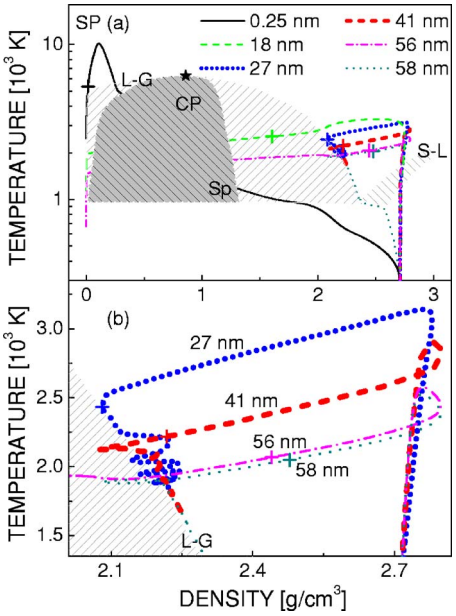


FIG. 10. (Color online) (a) Thermodynamic trajectories of several simulation cells in the excited aluminum region in a ($\rho$-$T$) diagram for a 180 fs laser pulse. The simulation ends at 5 ns. The electron-ion thermalization moment (+) is indicated in the figure for each trajectory and corresponds to a delay of 12 ps with respect to the beginning of the laser pulse. Note the "trapped" liquid regions at 27 and 41 nm depth. The incident fluence value is 1 J/cm$^2$. The solid-liquid (S-L; melting), the liquid-gas (L-G; binodal), and the onset of instabilities (Sp; spinodal) boundaries given by the EOS, as well as the position of the critical point (CP) are also depicted in the figure. Due to the uncertainty related to the passage via the instability region, the thermodynamic trajectories are not shown below the spinodal envelope. (b) Blow-up of the "trapped" region emphasizing the 27 and 41 nm trajectories. 56 and 58 nm are also shown.

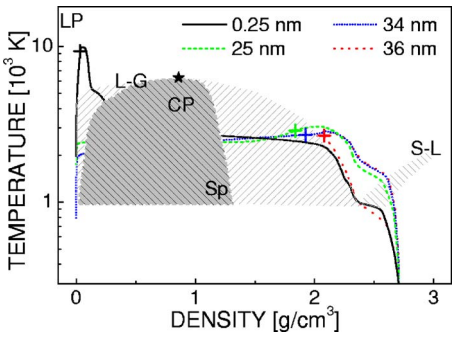


FIG. 11. (Color online) Thermodynamic trajectories of several simulation cells in the excited Al region in a ($\rho$-$T$) diagram for a 15 ps laser pulse. The simulation ends at 5 ns. The electron-ion thermalization moment is indicated in the figure and corresponds to the end of the laser pulse, at 45 ps. The incident fluence value is 1 J/cm$^2$. The solid-liquid (S-L; melting), the liquid-gas (L-G; binodal), and the onset of instabilities (Sp; spinodal) boundaries given by the EOS, as well as the position of the critical point (CP) are also depicted in the figure. Due to the uncertainty related to the passage via the instability region, the thermodynamic trajectories are not shown below the spinodal envelope.

cially pursuing an imposed monotonous path in the simulation, and, therefore, this is not a source of additional fluctuations.[74] Due to the uncertainty related to the passage via the instability region, the thermodynamic trajectories are not shown below the spinodal envelope, but the passage via the metastable and unstable regions takes about 15 ps and 200 ps, respectively (a finite lifetime in the unstable region appears due to the Maxwell construction of the passage).[74] This opens up the possibility of complementary nucleation mechanisms. It appears, therefore, from this behavioral path that a liquid layer, which does not expand as a gas, remains confined between these two gas bubbles in a sandwichlike structure. In this confined shell, hydrodynamic expansion is strongly limited and is insufficient by far to cool down the liquid. Deeper cells, such as the one at 58 nm (dotted line), remain no longer liquid and undergo liquid-solid transformation during the first nanosecond following the irradiation. The resolidification process occurs for all liquid cells located below this depth.

Observing in more detail the behavior of the liquid shell and its surrounding cells, particular features appear in the thermodynamic diagram. For all the cells in question except the first monolayer, the heating is quasi-isochoric and the temperature presents a vertical transition in the diagram. A temperature between 2000 and 3000 K is then observed in this case for the dotted and the short-dashed curves at 27 and 41 nm, respectively. A compression wave[51] is responsible for the appearance of overdense material in the liquid state. This is particularly visible in the behavior of the simulation cells at characteristic depths of 41, 56, and 58 nm. This mechanical wave is followed by a rarefaction wave which produces expansion almost independently of the temperature gain in this particular space, but strong expansion is limited to the region around 56 nm (between 55 and 57 nm) and does not affect a wider zone. A loop is clearly visible on the diagram when the shocked material begins its expansion [Fig. 10(b)]. The rarefaction wave induces matter expansion within the liquid layer and the decrease in density following expansion is not compensated by the density increase due to a fall in temperature. Consequently, the temperature and the density reductions are simultaneous in the liquid. This relaxation behavior, characteristic for isochoric heating, is favorable to start the liquid-gas transition at this depth and to form a localized "fracture" line. The transition occurs at a lower temperature than the maximal value reached at this specific location. In fact, the thermodynamic path approaches quasiperpendicularly the binodal line and it may cross the equilibrium border if the expansion is sufficient. As seen in Figs. 8 and 10, the process in question takes place in an internal zone of the liquid layer, at 56 nm in our case, where the liquid-gas transformation localized within the liquid layer is initiated. The liquid layer situated between this depth and the one corresponding to the limit of surface vaporization (18 nm) is not affected by the transformation, due to the fact that expansion is still insufficient. Consequently, the liquid layer remains trapped between the surrounding gas 1D bubbles during expansion and will contribute to the overall ablation process. In the physical reality, the exfoliation of the liquid layer can be considered as being triggered by the reflection of the rarefaction shock wave from the nonablated interface whenever the strength due to hydrodynamic motion begins to be comparable with the surface tension. The situation presented above can be followed in Fig. 10(a) and 10(b) where simulation shows confined thermodynamic paths for cells between 18 and 56 nm (limits not included), similar to the trajectories for the 27 and 41 nm cells. These cells are oscillating at the liquid-gas border for more than 5 ns; the moment which marks the termination of the calculations. Simulations indicate a liquid thickness of 38 nm which is consistent with the characteristic minimal dimension of a liquid droplet. This size is larger than the thickness of the vaporized material and, at this fluence not far away from the threshold, droplet ejection is clearly a major process of material removal. No direct solid-to-plasma transition is observed in this fluence regime since the material compression is not sufficient to bypass the solid-to-liquid transformation curve.

The situation changes drastically for the longer pulse sequence. For LP, evaporation occurs from a larger volume below the surface (since generally, ablation also involves liquid expulsion, this does not lead automatically to higher ablation rates, but to different plume composition) and the liquid-gas transition takes place through 34 nm of metal thickness. The internal energy is higher in this case because less energy is converted into mechanical (hydrodynamic) work during the slower heating. The cells trajectories presented in Fig. 11 show that the temperature increase is associated with a density decrease. The reason can be found in the fact that the expansion occurs during the energy transfer established by the laser energy coupling time and, as a consequence of the synchronous motion, confinement conditions are not fulfilled. Liquid phase appears to be a transient process in the simulation, and cells evolve rapidly towards either solid or gas states. The liquid layer does not survive in this case and no droplet formation and ejection is conceivable for longer pulse under the present irradiation conditions.

Under the last vaporized cell at 34 nm (short-dotted line), the cooling associated to the subsequent density increase induces the solidification of the liquid. The hydrodynamic expansion does not occur in the liquid phase and the cell (e.g. at 36 nm) shows a thermodynamic path which is parallel to the binodal line. No crossing is possible without sufficient expansion and the rarefaction wave does not compensate for the densification produced by the temperature decrease. Consequently, calculations indicate that if the maximum temperature achieved is not sufficient to kick start the liquid-gas transition, then the liquid layer returns to the solid state. Two kinds of behavior are distinguishable, a solid-liquid-gas transformation during pulse laser heating and a solid-liquid-solid transformation at the end of the heating cycle, since the temperature and density conditions for liquid-gas transition inside the liquid layer were not reached. These features are spatially separated, with little cross talking. To conclude, simulations reveal that the expansion in the liquid phase is weaker in this long exposure regime and the ablation is mainly due to vaporization. Even if this process is more important for the longer pulse and concerns the first 34 nm of the material, the ablated matter represents only 60% of the matter ejected by a short pulse. A thicker recast layer is predicted. We here note that a transition from a bubblelike expanding material involving liquid droplets to a diffusionlike beam upon the passage from femtosecond to picosecond irradiation has been recently described[42] based on combined Monte Carlo and molecular dynamics simulations of laser-excited silicon.

## V. THEORETICAL DESCRIPTION OF THE EXPERIMENTAL SITUATION

One of the important issues related to the evaluation of the experimental observations from Sec. II is to establish the corresponding domain of simulated fluences. One can reasonably suggest a connection between the experimental ion emission threshold (average fluence $F_{th-exp}=0.15$ J/cm$^2$) and the theoretical fluence required for material transformation in gas phase in the first surface layers ($F_{th-sim}=0.45$ J/cm$^2$).[75] Above this theoretical fluence, the first liquid layer confined between gas bubbles is formed for the short pulse sequence. To establish the matter behavior at $3F_{th-sim}$, we have extended the theoretical observations to fluences below and above this particular value and focused our attention on two relevant parameters of the interaction: the maximum temperature and the gas/liquid content of the ablated plume. We consider in the following that the departing liquid is formed only by one-dimensional droplets confined between gas bubbles. Although the evolution of the liquid droplets is not followed on longer space and time scales in order to decide if they will evaporate or break away in smaller droplets, these simulations pinpoint a possible source for these nanodroplets, i.e., the conditions for original liquid-phase expulsion (an intrinsic consequence of the short pulse action). Figure 12 shows in this respect the thermodynamic behavior and the evolution of these parameters in the selected fluence range. One can directly notice that, in conditions similar to the experimental situation, the LP induces, contrary to the SP pulse, a more efficient heating of the surface [Fig. 12(a)], opening pathways to supercritical states and to a preferential gas-phase transformation. Consequently, this leads to a significant decrease in the liquid content of the ablation plume [Fig. 12(b)] on the benefit of a hot gas phase. These aspects may have additional consequences for the subsequent plume evolution by promoting further collision driven acceleration during kinetic equilibration of the particles in the plume (similar to a Knudsen layer effect in the case of surface vaporization). These observations are in reasonable agreement with the experimental facts which predicted the appearance of a higher ion yield at high velocities. This can be partially deductible from Fig. 7 which shows the maximum velocity attained by the expanding layers at different input fluences. The maximum fluid velocity is always superior for the LP sequence as compared to the SP sequence for fluences above 1.2 J/cm$^2$. The statement covers the experimental situation as well; nevertheless, direct quantitative association to the TOF traces cannot be made since the trace characteristics are smeared out by the subsequent gas-phase dynamics. The acceleration takes place at the same time with a drastic reduction in the quantity of laser-generated nanodroplets. The liquid content of the plume goes down with increasing laser fluence. It is worth mentioning in this context that Vidal *et al.*[76] predict a fluence-independent liquid ratio of about 0.15 for a wide range of input intensities. This quantity is derived from the rate of erratic behavior of the simulation cells which preserve a high density after entering into the unstable zone below the critical point. This prediction, based on numerical oscillations, is supposed to be representative of the fluctuations occurring during phase transformation. We would ex-

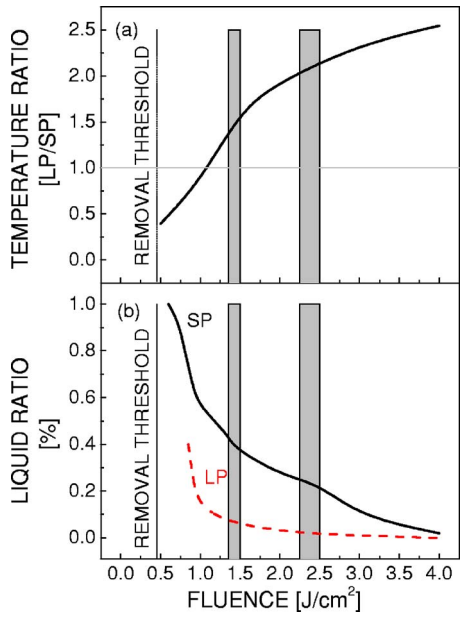


FIG. 12. (Color online) (a) The ratio between the maximum surface temperature achieved by LP and SP sequences at different input fluences. (b) The relative liquid content (confined liquid/gas +confined liquid) of the plume for SP and LP sequences at different input fluences. Only the confined liquid droplets are taken into consideration. The corresponding experimental fluence ranges at $3F_{th}$ and $5F_{th}$ are marked in both figures.

pect that this effect cannot be properly described in the frames of hydrodynamics without adequate nucleation theory and we suggest that this measure of the liquid part is only approximate and should depend on the laser fluence.

To describe droplet generation by ultrafast laser excitation of metallic targets, investigation on the correlation between laser parameters and nanoparticles synthesis has been previously performed in the theoretical context of an adiabatic expansion following nonequilibrium absorption.[16] Our approach extends this numerical analysis with the use of similar absorption and heat diffusion models inserted into a nonequilibrium hydrodynamical code.

## VI. CONCLUSION

In conclusion, we have analyzed material transformations under sub-ps and ps near infrared laser irradiation in conditions common to ablation regimes, with emphasis on the requirements for optimal energy coupling. A primary observation relates to the fact that short light exposure is not always the most efficient way to store energy in the material. In this context, the results point out the role of thermal nonequilibrium between electrons and ions to level out heat loading for short pulses, either by enhanced diffusion or by preferential transfer in shock wave energy. Adaptive control of the laser pulse temporal shape enables the designing of the kinetic properties of the material removed under laser excitation, based on a user-imposed synchronization with the induced series of phase transformations. The thermodynamic states and the associated density variations during the laser exposure create the prerequisites for better absorbing and transporting the energy inside the exposed material. The energy delivery rate is identified as an essential factor that predetermines the specific material thermodynamic evolution and its particular pathways in the phase space. In both cases presented here, SP and LP, pulses shorter or comparable to the heat conduction time preserve strong heating rates. As compared to short pulse regimes, longer pulse sequences show an acceleration of the emitted charge particles and a reduction in nanoparticulates ejection for fluences several times superior to the ablation threshold. The numerical simulations show a high efficiency of material removal for the SP sequence, where a major component of the plume is formed by liquid droplets in the form of nanosized particulates. Long-living liquid layers evolve as such under gas confinement and are responsible for this ejection feature. Longer irradiation sequences will not meet the pressure and temperature conditions for the liquid confinement. They will form liquid regions that do not have enough energy to expand and will return with high probability to the solid state as recast. Therefore, ultrafast laser pulses are more attractive when the degree of precision in laser structuring is concerned. Longer pulses will, nevertheless, play a role in defining and tuning the plume properties for applications where plume characteristics are important; droplet-free pulse laser deposition and generation of nanoparticles with tailored dimensions. Finally, although repeatedly advocated for ultrashort pulse laser ablation, no direct solid-to-plasma transition is observed in either case for the fluence range employed, since the material compression is not enough to trigger a path bypassing the liquid phase border in the phase space. The final states are always mediated by a transient liquid state.

## ACKNOWLEDGMENTS

The authors would like to thank N. M. Bulgakova for fruitful discussions on several aspects of this work. Additionally, they would like to thank the LTB Lasertechnik Berlin for technical support. The financial support of GIP-ANR and the PICS 2005 programs is gratefully acknowledged.

*Also at Department of Physics, Free University of Berlin.
†Electronic address: razvan.stoian@univ-st-etienne.fr

[1] B. N. Chichkov, C. Momma, S. Nolte, F. von Alvensleben, and A. Tünnermann, Appl. Phys. A: Mater. Sci. Process. **63**, 109 (1996).
[2] A. Semerok, C. Chaléard, V. Detalle, J.-L. Lacour, P. Mauchien, P. Meynadier, C. Nouvellon, B. Sallé, P. Palianov, M. Perdrix, and G. Petite, Appl. Surf. Sci. **138-139**, 311 (1999).
[3] J. Hohlfeld, S.-S. Wellershoff, J. Güdde, U. Conrad, V. Jähnke, and E. Matthias, Chem. Phys. **251**, 237 (2000).
[4] D. J. Funk, D. S. Moore, S. D. McGrane, J. H. Reho, and R. L. Rabie, Appl. Phys. A: Mater. Sci. Process. **81**, 295 (2005).
[5] K. T. Gahagan, D. S. Moore, D. J. Funk, R. L. Rabie, S. J. Buelow, and J. W. Nicholson, Phys. Rev. Lett. **85**, 3205 (2000).
[6] Ph. Rohwetter, J. Yu, G. Méjean, K. Stelmaszczyk, E. Salmon, J. Kasparian, J.-P. Wolf, and L. Wöste, J. Anal. At. Spectrom. **19**, 437 (2004).
[7] Y. Okano, H. Kishimura, Y. Hironaka, K. Nakamura, and K. Kondo, Appl. Surf. Sci. **197-198**, 281 (2002).
[8] D. Grojo, J. Hermann, and A. Perrone, J. Appl. Phys. **97**, 063306 (2005).
[9] J. König, S. Nolte, and A. Tünnermann, Opt. Express **13**, 10597 (2005).
[10] M. Ye and C. P. Grigoropoulos, J. Appl. Phys. **89**, 5183 (2001).
[11] O. Albert, S. Roger, Y. Glinec, J. C. Loulergue, J. Etchepare, C. Boulmer-Leborgne, J. Perrière, and E. Millon, Appl. Phys. A: Mater. Sci. Process. **76**, 319 (2003).
[12] R. Teghil, L. D'Alession, A. Santagata, M. Zaccagnino, D. Ferro, and D. J. Sordelet, Appl. Surf. Sci. **210**, 307 (2003).
[13] S. Amoruso, G. Ausanio, A. C. Barone, R. Bruzzese, L. Gragnaniello, M. Vitiello, and X. Wang, J. Phys. B **38**, L329 (2005).
[14] N. Benchikh, F. Garrelie, C. Donnet, K. Wolski, R. Y. Fillit, F. Rogemond, J. L. Subtil, J. N. Rouzaud, and J. Y. Laval, Surf. Coat. Technol. **200**, 6272 (2006).
[15] T. E. Glover, J. Opt. Soc. Am. B **20**, 125 (2003).
[16] S. Eliezer, N. Eliaz, E. Grossman, D. Fisher, I. Gouzman, Z. Henis, S. Pecker, Y. Horovitz, M. Fraenkel, S. Maman, and Y. Lereah, Phys. Rev. B **69**, 144119 (2004).
[17] R. Le Harzic, N. Huot, E. Audouard, C. Jonin, P. Laporte, S. Valette, A. Fraczkiewicz, and R. Fortunier, Appl. Phys. Lett. **80**,

3886 (2002).
[18] A. Y. Vorobyev and C. Guo, Appl. Phys. Lett. **86**, 011916 (2005).
[19] P. B. Corkum, F. Brunel, N. K. Sherman, and T. Srinivasan-Rao, Phys. Rev. Lett. **61**, 2886 (1988).
[20] E. G. Gamaly, A. V. Rode, B. Luther-Davies, and V. T. Tikhonchuk, Phys. Plasmas **9**, 949 (2002).
[21] A. P. Kanavin, I. V. Smetanin, V. A. Isakov, Yu. V. Afanasiev, B. N. Chichkov, B. Wellegehausen, S. Nolte, C. Momma, and A. Tünnermann, Phys. Rev. B **57**, 14698 (1998).
[22] R. S. Judson and H. Rabitz, Phys. Rev. Lett. **68**, 1500 (1992).
[23] D. Meshulach and Y. Silberberg, Nature (London) **396**, 239 (1998).
[24] A. Assion, T. Baumert, M. Bergt, T. Brixner, B. Kiefer, V. Seyfried, M. Strehle, and G. Gerber, Science **282**, 919 (1998).
[25] A. Lindinger, C. Lupulescu, M. Plewicki, F. Vetter, A. Merli, S. M. Weber, and L. Wöste, Phys. Rev. Lett. **93**, 033001 (2004).
[26] A. M. Weiner, Rev. Sci. Instrum. **71**, 1929 (2000).
[27] R. Stoian, Ph.D. thesis, Free University Berlin, 2000.
[28] M. M. Wefers and K. A. Nelson, J. Opt. Soc. Am. B **12**, 1343 (1995).
[29] T. Tanabe, F. Kannari, F. Korte, J. Koch, and B. Chichkov, Appl. Opt. **44**, 1092 (2005).
[30] H. Varel, M. Wähmer, A. Rosenfeld, D. Ashkenasi, and E. E. B. Campbell, Appl. Surf. Sci. **127-129**, 128 (1998).
[31] R. Stoian, A. Mermillod-Blondin, N. M. Bulgakova, A. Rosenfeld, I. V. Hertel, M. Spyridaki, E. Koudoumas, P. Tzanetakis, and C. Fotakis, Appl. Phys. Lett. **87**, 124105 (2005).
[32] D. Perez and L. J. Lewis, Phys. Rev. B **67**, 184102 (2003).
[33] P. Lorazo, L. J. Lewis, and M. Meunier, Phys. Rev. Lett. **91**, 225502 (2003).
[34] A. Bartelt, Ph.D. thesis, Freie Universität Berlin, 2002.
[35] L. V. Zhigilei and B. J. Garrison, Appl. Phys. Lett. **71**, 551 (1997).
[36] X. Y. Wang and M. C. Downers, Opt. Lett. **17**, 1450 (1992).
[37] A. Semerok and C. Dutouquet, Thin Solid Films **453-454**, 501 (2004).
[38] B. Rethfeld, K. Sokolowski-Tinten, D. von der Linde, and S. I. Anisimov, Phys. Rev. B **65**, 092103 (2002).
[39] H. Ki, P. S. Mohanty, and J. Mazumder, J. Phys. D **34**, 364 (2001).
[40] C. Schäfer, H. M. Urbassek, and L. V. Zhigilei, Phys. Rev. B **66**, 115404 (2002).
[41] T. E. Itina, J. Hermann, Ph. Delaporte, and M. Sentis, Thin Solid Films **453-454**, 513 (2004).
[42] P. Lorazo, L. J. Lewis, and M. Meunier, Phys. Rev. B **73**, 134108 (2006).
[43] A. V. Bushman, I. V. Lomonosov, and V. E. Fortov, Sov. Technol. Rev. B **5**, 1 (1993).
[44] S. Fähler, M. Störmer, and H. U. Krebs, Appl. Surf. Sci. **109-110**, 433 (1997).
[45] N. Seifert, G. Betz, and W. Husinsky, Appl. Surf. Sci. **103**, 63 (1996).
[46] I. Weaver and C. L. S. Lewis, Appl. Surf. Sci. **96-98**, 663 (1996).
[47] A. V. Bulgakov, I. Ozerov, and W. Marine, Thin Solid Films **453-454**, 557 (2004).
[48] S. H. Jeong, R. Greif, and R. E. Russo, Appl. Surf. Sci. **127-129**, 177 (1998).
[49] N. Y. Bykov, N. M. Bulgakova, A. V. Bulgakov, and G. A. Loukianov, Appl. Phys. A: Mater. Sci. Process. **79**, 1097 (2004).
[50] A. Miotello and R. Kelly, Appl. Phys. Lett. **67**, 3535 (1995).
[51] J. P. Colombier, P. Combis, F. Bonneau, R. Le Harzic, and E. Audouard, Phys. Rev. B **71**, 165406 (2005).
[52] S.-S. Wellershoff, J. Hohlfeld, J. Güdde, and E. Matthias, Appl. Phys. A: Mater. Sci. Process. **69**, S99 (1999).
[53] M. I. Kaganov, I. M. Lifshitz, and L. V. Tanatarov, Zh. Eksp. Teor. Fiz. **31**, 232 (1956) [Sov. Phys. JETP **4**, 173 (1957)].
[54] S. I. Anisimov, B. Kapeliovich, and T. L. Perel'man, Zh. Eksp. Teor. Fiz. **66**, 776 (1974) [Sov. Phys. JETP **39**, 375 (1974)].
[55] N. K. Sherman, F. Brunel, P. B. Corkum, and F. A. Hegmann, Opt. Eng. **28**, 1114 (1989).
[56] P. Celliers and A. Ng, Phys. Rev. E **47**, 3547 (1993).
[57] R. W. Schoenlein, W. Z. Lin, J. G. Fujimoto, and G. L. Eesley, Phys. Rev. Lett. **58**, 1680 (1987).
[58] V. E. Gusev and O. B. Wright, Phys. Rev. B **57**, 2878 (1998).
[59] D. Bejan and G. Raseev, Phys. Rev. B **55**, 4250 (1997).
[60] W. Ebeling, A. Förster, V. Fortov, V. Griaznov, and A. Polishchuk, *Thermophysical Properties of Hot Dense Plasmas* (Teubner, Stuttgart, 1991).
[61] E. Palik, *Handbook of Optical Constants of Solids* (Academic, London, 1985).
[62] P. Drude, Ann. Phys. **1**, 566 (1900).
[63] P. L. Silvestrelli, Phys. Rev. B **60**, 16382 (1999).
[64] D. Fisher, M. Fraenkel, Z. Henis, E. Moshe, and S. Eliezer, Phys. Rev. E **65**, 016409 (2001).
[65] N. W. Ashcroft and K. Sturm, Phys. Rev. B **3**, 1898 (1971).
[66] S. Krishnan and P. C. Nordine, Phys. Rev. B **47**, 11780 (1993).
[67] H. M. Milchberg, R. R. Freeman, S. C. Davey, and R. M. More, Phys. Rev. Lett. **61**, 2364 (1988).
[68] Y. B. Zel'dovich and O. M. Todes, Zh. Eksp. Teor. Fiz. **10**, 1441 (1940).
[69] K. Sokolowski-Tinten, J. Bialkowski, A. Cavalleri, D. von der Linde, A. Oparin, J. Meyer-ter-Vehn, and S. I. Anisimov, Phys. Rev. Lett. **81**, 224 (1998).
[70] A. M. Komashko, M. D. Feit, A. M. Rubenchik, M. D. Perry, and P. S. Banks, Appl. Phys. A: Mater. Sci. Process. **69**, Suppl. S95 (1999).
[71] The border between the ejected matter and the remaining solid is difficult to access in a one-dimensional hydrodynamic treatment. Due to a lack of information on the nucleation mechanisms and considerations of bubble growth, no clear separation between ablated and nonablated matter can be defined. A criterion based on thermodynamic estimations but stripped of kinetic considerations is usually employed to estimate the ablation rate and the ablated limit is considered to occur at the solid-fluid interface. Alternatively, a second criterion may be defined. The accelerated liquid layer may be considered as ejected from the sample in the simulation timescale and the resolidification process would concern a thinner liquid layer than expected. This point has already been discussed in the context of hydrodynamic codes (see, e.g., Refs. 51 and 70) and is beyond the scope of this work. Based on the former criterion, one can foresee a rapid growth of the ablation rate with the input fluence, surpassing the SP rate at a fluence around 1.5 $J/cm^2$.
[72] This behavior can be attributed to the electron-ion energy relaxation occurring during the expansion of the hot electron gas. The electron-phonon coupling constant depends strongly on the electronic structure and its value is known with low accuracy at standard conditions. The linear dependence with the difference in the electron and the ion temperature is supposed to be valid for a weak variation at solid density. For lower densities, the

plasma model should be applied but the extension of this model to high densities is not self-consistent with the solid model and leads to an overestimation of the coupling coefficient [see, e.g., A. Ng, A. Forsman, and P. Celliers, Phys. Rev. E **51**, R5208 (1995)]. To avoid increasing the complexity in our simulations, the electron-phonon coupling constant is left as a parameter with a constant value. If this assumption is acceptable during the quasi-isochoric heating, its accuracy may be doubtful during gas expansion (when insulating phases may appear). This fact is responsible for thermodynamic paths where the maximum temperature is reached at a density lower than the one corresponding to the critical point. However, this uncertainty on the thermalization time concerns few cells, as the external one at 0.25 nm in Figs. 10 and 11, and we suppose that the global thermodynamic behavior of the material is reasonable.

[73] N. M. Bulgakova, I. M. Bourakov, and N. A. Bulgakova, Phys. Rev. E **63**, 046311 (2001).

[74] In an equilibrium description of a thermodynamic system, long-lived metastable states may appear as local extreme points of a certain free energy. For such systems, the equilibrium isotherms below the critical temperature show metastable branches, corresponding to those extreme points where the end values are called spinodal points. The region where those local extreme points may appear is still a matter of debate, and the properties of the mechanically unstable regions are not dissociated from the ones of the stable regions in the EOS employed in this work. Moreover, a plateau corresponding to the Maxwell construction of the isotherms appears in the region of the temperature-specific energy diagram where nucleation theory plays a major role, particularly for a nonequilibrium system. This standard construction preserves our numerical calculations from potential instabilities which may occur with van der Waals type EOS.

[75] S. Petzoldt, J. Reif, and E. Matthias, Appl. Surf. Sci. **96-98**, 199 (1996).

[76] F. Vidal, T. W. Johnston, S. Laville, O. Barthélemy, M. Chaker, B. Le Drogoff, J. Margot, and M. Sabsabi, Phys. Rev. Lett. **86**, 2573 (2001).